



ELSEVIER

Available online at www.sciencedirect.com

SCIENCE @ DIRECT®

EPSL

Earth and Planetary Science Letters 218 (2004) 475–490

www.elsevier.com/locate/epsl

A Late Neoproterozoic (~ 630 Ma) high-magnesium andesite suite from southern Israel: implications for the consolidation of Gondwanaland

O. Katz^a, M. Beyth^a, N. Miller^c, R. Stern^{c,*}, D. Avigad^b, A. Basu^d,
A. Anbar^d

^a Geological Survey of Israel, 30 Malkhe Yisrael Street, Jerusalem 95501, Israel

^b Institute of Earth Sciences, The Hebrew University of Jerusalem, Jerusalem 91904, Israel

^c Geosciences Department, University of Texas at Dallas, Box 830688, Richardson, TX 75083-0688, USA

^d Department of Earth and Environmental Sciences, University of Rochester, Rochester, NY 14627, USA

Received 8 July 2003; received in revised form 15 September 2003; accepted 30 October 2003

Abstract

The East African Orogen formed as a result of collision between portions of East and West Gondwanaland as the Mozambique Ocean closed in Late Neoproterozoic time, but it is not known exactly when. We use distinctive chemical and isotopic composition of deformed ‘schistose’ dykes in southern Israel to argue that this collision occurred after about 630 Ma, when the dykes were emplaced. These magmas had compositions of basaltic andesites and andesites but had high Mg# (100 Mg/Mg+Fe; 55–70 ppm), Ni (70–240 ppm), and Cr (100–400 ppm) indicating that the most primitive samples were in equilibrium with mantle peridotite; evolved samples suffered modest fractionation. The schistose dykes are a medium-K, calc-alkaline suite, strongly enriched in light rare earth elements and depleted in heavy rare earth elements. They are high-magnesium andesites and are similar to low-Ca type 2 boninites; similar magmas today only form over active subduction zones. The schistose dykes have non-radiogenic initial $^{87}\text{Sr}/^{86}\text{Sr}$ (0.7026–0.7033) and radiogenic $^{143}\text{Nd}/^{144}\text{Nd}$, with $\epsilon_{\text{Nd}}(630 \text{ Ma})$ of +2.7 to +4.9 and $T_{\text{DM}} = 0.77\text{--}0.94$ Ga. Hf isotopic compositions ($\epsilon_{\text{Hf}}(630 \text{ Ma}) = +6.8$ to +8.8) confirm the juvenile nature of these magmas. The dykes are closely related to a nearby quartz diorite, although it is not clear whether the dykes represent magma that fed into a magma body now filled with the quartz diorite, or issued from it. The generation of high-Mg andesite magma at 630 Ma involved reactive porous flow of a slab-derived melt through the mantle, requiring an active subduction zone, and strongly suggesting that young, hot seafloor – perhaps the spreading ridge of the Mozambique Ocean – was subducted. This indicates that collision between components of E. and W. Gondwana to form the East African Orogen must have occurred more recently than 630 Ma.

© 2003 Elsevier B.V. All rights reserved.

Keywords: East African Orogen; Arabian–Nubian Shield; Neoproterozoic; high-magnesium andesite

1. Introduction

The Arabian–Nubian Shield (ANS) comprises

* Corresponding author. Tel.: +1-972-8832401;

Fax: +1-972-8832537.

E-mail address: rjstern@utdallas.edu (R. Stern).

the northern segment of the East African Orogen (EAO). ANS crust reflects the growth and accretion of intraoceanic island arc systems – and perhaps oceanic plateaux – associated with the closing of the Mozambique Ocean during Neoproterozoic time. Juvenile ANS crust evolved to true continental crust as a result of crustal thickening and intracrustal differentiation, and this crust stands as one of the best examples of how juvenile continental crust forms as a consequence of plate tectonic processes [1]. The EAO records terminal collision between important parts of E. and W. Gondwana to form a supercontinent at the end of Neoproterozoic time, including crustal thickening to form vast granulite tracts in the south [2]. It also preserves a record of tectonic escape and orogenic collapse [3–7]. The northernmost EAO was particularly affected by strong extension at the end of the EAO tectonic cycle [8]. These magmatic and tectonic events may have contributed to major biological and climatic changes during Neoproterozoic time [9]. Cessation of igneous and tectonic activity at about the Cambrian–Precambrian boundary (~ 545 Ma) ushered in the platform stage [10], possibly associated with a newly developed passive margin truncating the northernmost EAO.

It is important for our understanding of Neoproterozoic Earth history to refine our understanding of the nature, significance, and timing of transitions between the various tectonic stages in the evolution of the ANS and EAO, and relate these to episodes of subduction, terrane accretion, continental collision, tectonic escape, and orogenic collapse. Garfunkel [10] identifies three tectonic stages in the evolution of the northernmost EAO: orogenic (> 600 Ma), transitional (600–530 Ma), and platform (< 530 Ma). The first two of these stages correspond to the ‘orogeny’ and ‘extension’ stages of Beyth et al. [11], the transition for which occurred about 610–625 Ma in Jordan, Israel, and E. Egypt. This is consistent with Ar thermochronometry results indicating that this region was deformed and metamorphosed at 620 ± 10 Ma followed by unroofing and cooling by about 600 Ma [12]. So defined, the orogenic stage does not resolve subduction, terrane accretion, and terminal collision phases. The subduction and terrane ac-

cretion phase occurred while the Mozambique Ocean was closing and during the interval 870–690 Ma [1]. This was followed by terminal collision between large parts of E. and W. Gondwanaland near the end of Neoproterozoic time. The timing of terminal collision is controversial (compare estimates of 750–650 Ma [1] and 650–620 Ma [13]). Recent dating of post-tectonic granites in Ethiopia at 613 ± 1 Ma and 606 ± 1 Ma indicates collision occurred in the southern ANS prior to 613 Ma [14].

It is clear that understanding the nature of the collision and the history of post-collisional convergence requires integrating a wide range of data from igneous, metamorphic, and sedimentary rocks over the entire EAO. Identifying and dating igneous rocks that formed at convergent plate boundaries can help constrain when the subduction phase ended and when the terminal collision phase began. Unfortunately, such interpretations can be controversial, as seen for the ~ 600 Ma Dokhan Volcanics of Egypt, variously interpreted as forming in a mature arc setting [15] or in a rift zone [16,17]. Such uncertainty near the time of transition can reflect the fact that mantle modified by subduction loses this chemical ‘memory’ slowly, over a few tens of millions of years after subduction ends [18].

Some igneous rock suites are diagnostic of primitive arc environments, and among these boninites and high-magnesium andesites (HMAs) stand out. Boninites and HMAs result from melting of the mantle wedge above an active or newly forming subduction zone; thus the existence of such rocks in ancient crustal tracts provides powerful constraints on when subduction occurred. In the following report we document a HMA suite from the Neoproterozoic of southern Israel for the first time and use these data to help understand the evolution of the ANS and EAO.

2. Geologic setting and previous work

Neoproterozoic basement is exposed in marginal uplifts on the flanks of the Red Sea (Fig. 1A), including in southern Israel (Fig. 1B). The base-

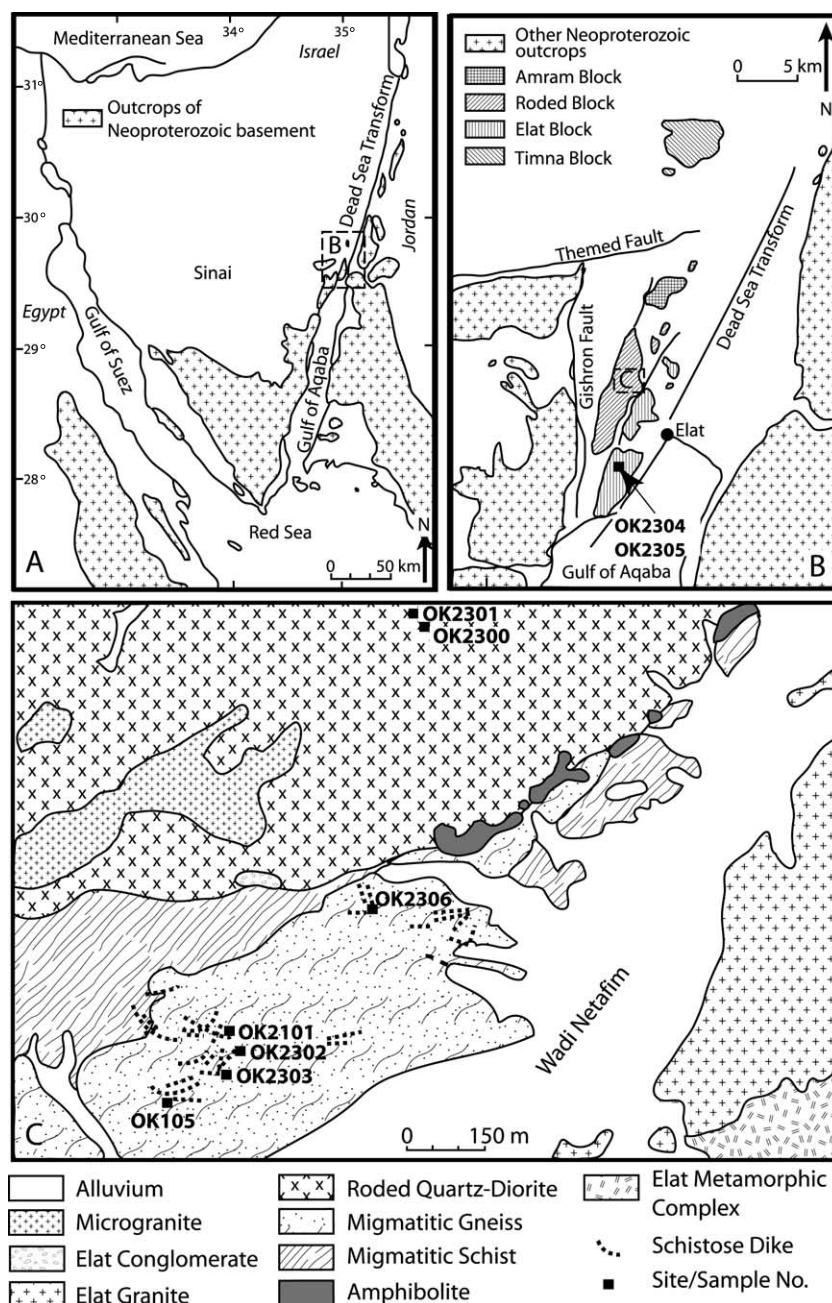


Fig. 1. Location maps. (A) Neoproterozoic basement exposures around the northern Red Sea. (B) Basement exposures of southern Israel and surrounding areas. Note that two of the samples analyzed in this study and all of the samples analyzed in [23] are from the southern Elat block. (C) Detail of the study area in the central Roded block. Modified after [19].

ment in southern Israel occurs in four fault-bounded blocks: Timna, Amran, Roded and Elat (Fig. 1B). The metamorphic sequence in the

eastern part of the Roded block is cut by two generations of metamorphosed and foliated mafic dykes [19,20], respectively concordant and discor-

dant to the metamorphic structure of the country rock ('schist dikes' of Bentor [21]). These 'schistose dykes' are abundant in the Elat and Roded blocks (Fig. 1B). They are mafic to intermediate in composition, and individual dykes can be traced for a few tens of meters up to 2 km [22]. The metamorphic grade of these dykes varies from greenschist to amphibolite facies [19].

Cohen [23] studied the schistose dykes of the Elat block (Fig. 1B) and concluded that the chemical composition of the original igneous rock was little changed during metamorphism, although hot fluids with high K content caused minor alteration mainly along the contact of the dyke with the host rock. She concluded that the original minerals were amphibole (kaersutite) and Na-plagioclase. She also suggested that this andesite was compositionally similar to modern andesite erupted in the Marianas Island Arc. Data for dykes analyzed by Cohen is plotted along with our results in Figs. 3 and 4.

Heiman et al. [24] concluded that schistose dykes in the Elat block were intruded after 640 Ma and before 580 Ma. They reported that amphibole separates from the schist dykes give variable total $^{40}\text{Ar}/^{39}\text{Ar}$ ages, ranging from 592 to

495 Ma. Highly chloritized biotites yield a 446 Ma total-gas age and its age spectrum shows a staircase pattern, with a maximum at approximately 610 Ma.

The schistose dykes are subdivided into an older set that is concordant with regional foliation and a younger set which is not. Concordant schistose dykes in the Roded block strike north–south and have vertical foliation planes and subhorizontal lineations, similar to structures in the host rock. The discordant dykes strike east–west and are characterized by a steep, sigmoidal foliation. This foliation suggests both strike-slip and normal displacement along the dyke walls. The E–W trending, discordant schistose dykes intrude the Roded quartz diorite, but the concordant schistose dykes do not. Since this quartz diorite yields a U–Pb zircon age of 634 ± 2 Ma [19] and a zircon evaporation age of 630 ± 3 Ma [25], the concordant schist dykes must have intruded prior to ~ 632 Ma and the discordant ones after ~ 632 Ma. Both generations of dykes are andesitic on the IUGS total alkalis vs. silica diagram [26]. The similar composition of discordant and concordant dykes, contradictory intrusive relationships with the quartz diorite, and the occurrence

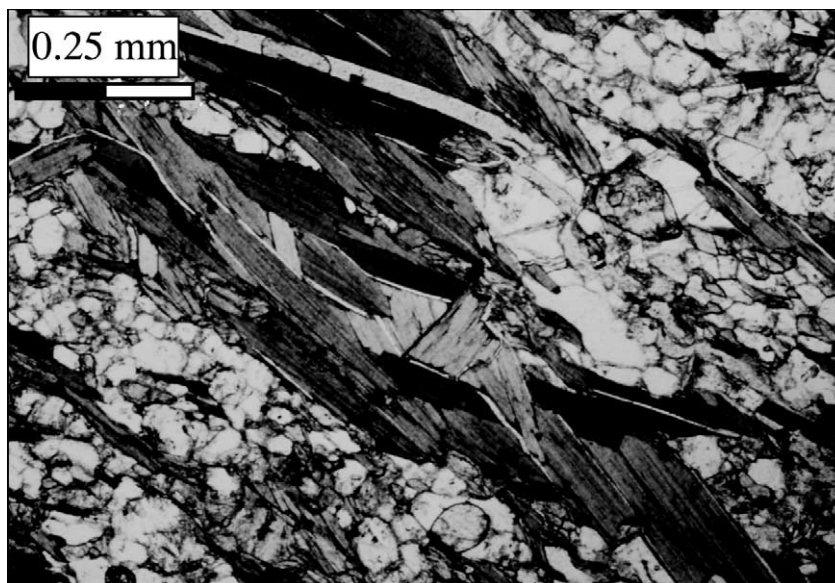


Fig. 2. Photomicrograph of a schistose dyke sample 105 showing a cluster of preferred oriented biotite prisms in a matrix of plagioclase and minor quartz crystals in polygonal texture. Biotite clusters define the foliation of the dykes.

of these units in a restricted area (similar dykes are unknown from adjacent regions in Jordan or Sinai) suggests a close relationship in time and space, with each other and with the Roded quartz diorite. This conclusion is supported by compositional and isotopic data presented in following sections. Katz et al. [19] noted that the concordant dykes are not consistent with peak metamorphic conditions suggesting that either these rocks underwent extensive retrograde recrystallization after peak of metamorphism or that they intruded later and underwent only lower grade of recrystallization'. We prefer the second possibility and conclude that discordant and concordant dykes intruded slightly after and before emplacement of the Roded quartz diorite about 632 Ma, respectively.

The schistose dyke mineral assemblage is dominated by amphibole and biotite, which form oriented clusters embedded in a polygonal textured matrix of plagioclase (andesine) and minor quartz (Fig. 2). Amphiboles in concordant schistose dykes from the Roded block are compositionally homogenous actinolites of the 'low-temperature' type. In contrast, amphiboles from the discordant schistose dykes are zoned with cores of magnesio-hornblende and magnesio-hastingsite of the 'high-temperature' magmatic type and the rims are magnesio-hornblende and actinolite of 'low-temperature' type typical of greenschist-facies metamorphic rocks. Amphibole–plagioclase thermometry of unzoned actinolitic amphiboles in the concordant schistose dykes gives equilibrium temperatures of $511 \pm 7^\circ\text{C}$. Amphibole–plagioclase thermometry of the discordant schistose dykes yields equilibrium temperatures of $650 \pm 20^\circ\text{C}$ for the cores and $575 \pm 15^\circ\text{C}$ for the rims [19]. These are not magmatic temperatures and presumably reflect partial re-equilibration of these minerals to metamorphic conditions.

3. Analytical techniques

Nine samples of discordant schistose dykes were utilized in this study: two from the Elat block (OK2304 and OK2305), and seven others from the Roded block (locations shown in

Fig. 1). Two samples (2300 and 2301) intrude the Roded quartz diorite.

The samples were crushed and fused with lithium metaborate and analyzed for major oxides by inductively coupled plasma-atomic emission spectrometry (ICP-AES) using the Perkin-Elmer Optima 3300 at the Geological Survey of Israel (GSI). Splits of samples were sintered with sodium peroxide (Na_2O_2) and analyzed for trace elements by ICP-AES using the JY-48 at the GSI. The samples were analyzed for rare earth elements (REE) using the Perkin-Elmer-SCIEX Elan 6000 ICP mass spectrometer (MS) at the GSI, except for Nd and Sm by isotope dilution at the University of Texas at Dallas (UTD). $^{87}\text{Sr}/^{86}\text{Sr}$ was determined using the Finnigan MAT 261 solid-source mass spectrometer at the UTD. Reproducibility of $^{87}\text{Sr}/^{86}\text{Sr}$ is ± 0.00004 . During the course of this work the UTD lab obtained a mean $^{87}\text{Sr}/^{86}\text{Sr} = 0.70803 \pm 3$ for several analyses of the E and A SrCO_3 standard; data reported here have been adjusted to correspond to a value of 0.70800 for the E and A standard. $^{143}\text{Nd}/^{144}\text{Nd}$ was also determined using the UTD Finnigan-MAT261 in the dynamic multicollector mode. Calculations of $\epsilon_{\text{Nd}(T)}$ were made assuming bulk earth $^{147}\text{Sm}/^{144}\text{Nd} = 0.1967$ and using values of ϵ_{Nd} for the UCSD standard (-15.2) and BCR (-0.16) [27]. A total range of ± 0.00002 observed for $^{143}\text{Nd}/^{144}\text{Nd}$ of the standard (mean value = 0.511868) is taken as the analytical uncertainty for the samples.

We measured the Hf isotopic compositions at the University of Rochester. The measurements were made statically on a VG Elemental Plasma 54, a multicollector, double-focusing magnetic sector mass spectrometer with an inductively coupled plasma source. Other clean-laboratory column chemistry and mass spectrometric data acquisition are the same as described by Blichert-Toft et al. [28]. We use the JMC-475 Hf standard to test reproducibility and accuracy. For a sample size of 500 ng our in-run precision (2 S.E.) on $^{176}\text{Hf}/^{177}\text{Hf}$ is between ± 0.000007 and ± 0.000011 , which is better than twice as good as that typically reported for the thermal ionization mass spectrometric method. All analyses were normalized to $^{179}\text{Hf}/^{177}\text{Hf} = 0.7325$. During the

Table 1
Major trace and REE contents of schistose dykes

Oxide/element	OK105	OK2101	OK2300	OK2301	OK2302	OK2303	OK2304	OK2305	OK2306
SiO ₂	57.0	56.8	58.5	58.0	56.2	59.0	54.7	60.1	60.4
Al ₂ O ₃	14.1	14.9	15.1	14.4	13.9	16.0	14.7	15.4	15.6
Fe ₂ O ₃	6.6	6.1	6.5	5.8	7.3	5.7	7.9	5.7	5.0
TiO ₂	0.8	1.0	1.1	0.7	1.1	1.0	1.1	0.9	0.9
CaO	5.9	5.9	5.6	5.7	6.7	5.2	7.0	4.8	4.7
MgO	7.9	5.3	5.1	6.9	6.7	3.6	6.9	4.6	4.5
MnO	0.1	0.1	0.1	0.1	0.1	0.1	0.1	0.1	0.1
P ₂ O ₅	0.3	0.6	0.6	0.4	0.6	0.7	0.6	0.6	0.6
SO ₃	0.1	<0.1	<0.1	<0.1	<0.1	<0.1	<0.1	<0.1	<0.1
Na ₂ O	3.8	3.3	3.8	3.6	3.5	4.4	3.3	4.7	4.6
K ₂ O	1.7	1.1	2.0	2.1	1.5	1.5	1.6	1.6	1.3
LOI	1.9	5.4	1.4	1.9	2.5	2.9	2.0	1.9	2.6
Total	100.2	100.5	99.8	99.6	100.1	100.1	99.9	100.4	100.3
Mg#	70.3	63.3	60.9	70.2	64.5	55.6	63.4	61.5	64.1
CaO/Al ₂ O ₃	0.418	0.396	0.371	0.396	0.482	0.325	0.476	0.312	0.301
Na ₂ O/K ₂ O	2.24	3.00	1.90	1.71	2.33	2.93	2.06	2.94	3.54
Rb (ppm)	35	66	32	45	29	26	50	41	24
Ba	550	365	800	660	630	730	458	700	640
Th	3.0	3.3	2.4	2.7	2.9	3.8	3.3	3.2	3.1
U	1.1	1.8	0.8	0.7	1.6	2.7	0.9	1.0	1.8
Sr	700	780	925	800	1050	900	925	900	860
Pb	8	15	7	7	7	9	9	12	8
Nb	5	7	8	4	6	6	6	5	8
Ta	0	1	1	0	0	0	0	0	0
Cr	400	185	160	360	280	100	210	195	180
Ni	240	140	70	200	145	60	120	90	110
Zn	70	115	75	80	85	80	110	90	80
Cd	0	1	0	0	0	0	0	1	0
Cu	29	51	33	41	10	61	35	46	17
Co	30	28	29	31	29	21	30	25	24
V	135	25	160	130	155	120	190	110	90
Zr	110	150	140	140	140	160	150	160	190
Y	9	13	17	13	11	12	17	12	9
La	16	25	23	19	22	23	22	22	20
Ce	36	58	60	43	50	52	53	51	45
Nd	23.8	36.9	35.0	22.6	34.7	32.4	38.7	30.9	28.7
Sm	4.2	7.0	6.8	4.4	6.2	6.1	7.7	5.9	5.2
Eu	0.9	1.6	1.8	1.2	1.3	1.4	1.8	1.4	1.0
Gd	2.7	4.1	4.9	3.5	3.6	3.8	4.6	3.7	2.9
Tb	0.39	0.58	0.73	0.53	0.49	0.52	0.68	0.51	0.41
Dy	1.8	2.7	3.4	2.6	2.2	2.4	3.3	2.3	1.8
Ho	0.33	0.48	0.61	0.47	0.40	0.43	0.61	0.40	0.31
Er	1.0	1.4	1.8	1.4	1.2	1.2	1.7	1.2	0.9
Tm	0.15	0.20	0.28	0.22	0.18	0.19	0.26	0.18	0.14
Yb	0.77	1.09	1.46	1.12	0.96	0.97	1.37	1.00	0.74
Lu	0.11	0.16	0.21	0.17	0.13	0.14	0.21	0.14	0.11

course of these measurements the JMC-475 Hf standard values were: $^{176}\text{Hf}/^{177}\text{Hf} = 0.282166 \pm 20$ ($N=11$). Lu and Hf concentrations were determined with a quadrupole ICP-MS using multiple silicate rock standards; errors associated with these measurements were usually less than 3%. In estimating the initial ϵ_{Hf} values in Table 4, we used the bulk earth chondritic $^{176}\text{Hf}/^{177}\text{Hf}$ value of 0.282772 and $^{176}\text{Lu}/^{177}\text{Hf} = 0.0332$.

4. Results

Major and trace element results are listed in Table 1. The schistose dykes are basaltic-andesite to andesite in composition (Fig. 3, top panel) and have strong calc-alkaline affinities (Fig. 3, bottom panel). All of the samples that we have analyzed as well as the Roded quartz diorite plot in the

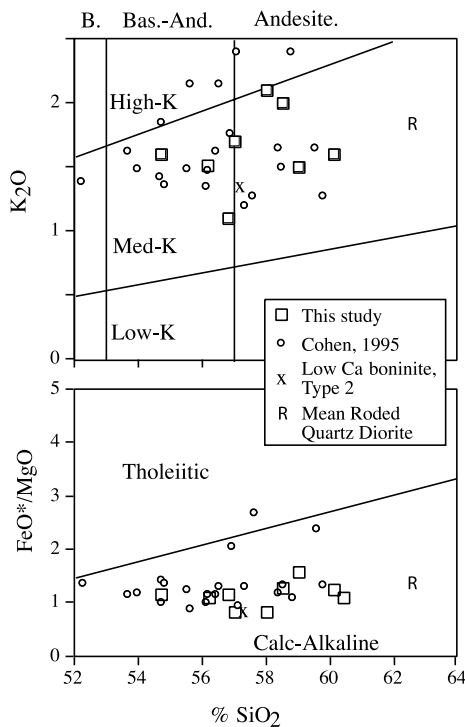


Fig. 3. Major element characterization of the schistose dykes from this study and that of [23]. Top panel: K_2O – SiO_2 diagram [53]; B = basalt. Bottom panel: FeO^*/MgO – SiO_2 diagram, modified after [54]. Mean composition of low-Ca boninite type 2 and mean Roded quartz diorite from Table 4.

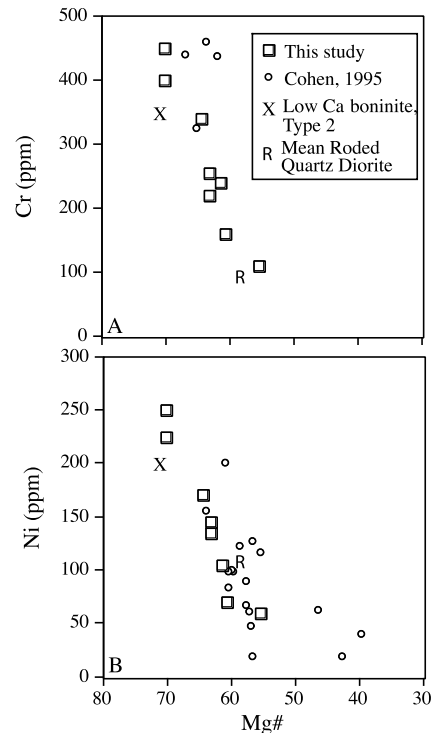


Fig. 4. Relative abundances of compatible ferromagnesian elements relative to Mg#. (A) Cr; (B) Ni. Mean composition of low-Ca boninite type 2 and mean Roded quartz diorite from Table 4.

low-Fe field for subalkaline igneous rocks [29]. On the K_2O – SiO_2 diagram, our samples plot in the medium-K field, although a few of the samples analyzed by Cohen [23] plot in the high-K field (Fig. 3, top panel). CIPW norms contain 5–14% quartz and 11–20% hypersthene; normative plagioclase is AN_{28} to AN_{43} . Most of the schistose dykes are enriched in MgO , containing between 3.6 and 7.9% with an average of 5.7% MgO (Table 1). Mg\# ($100 \text{ Mg}/(\text{Mg} + \text{Fe})$) varies between 70.3 and 55.6 with an average of 63.8. Except for sample OK2303, all the samples have $\text{Mg\#} > 61$ and two samples (OK105 and OK2301) have $\text{Mg\#} > 70$. This is a conservative estimate of Mg\# , because we calculate all iron as Fe, whereas magmatic $\text{Fe}_2\text{O}_3/\text{FeO}$ for andesitic magmas is probably close to 0.3 [30]. More realistic estimates of magmatic Mg\# (assigning 80% of total Fe to Fe^{+2}) yield Mg\# that are 8–10% higher than those listed in Table 1, with an aver-

age Mg# of 69. Regardless, samples with the higher Mg# are in equilibrium with mantle peridotite. All samples are enriched in Ni (average 143 ppm) and Cr (average 264 ppm). There is a clear correlation between high Ni and Cr and high Mg# (Fig. 4), suggesting control by fractionation of mafic phases.

Na₂O/K₂O ranges from 1.7 to 3.5, with a mean of 2.5; this is similar to values for juvenile, intra-oceanic arcs [31]. Some of the variability in Na₂O/K₂O is likely due to post-emplacement alteration, but the relatively restricted range in this ratio and its similarity to that of modern arc lavas suggests that alteration had a modest effect on even the alkali metals. CaO/Al₂O₃ ranges from 0.30 to 0.48 with a mean of 0.38 (Table 1). CaO/Al₂O₃ is low relative to lherzolite melts, typically ~0.79 for basalts such as mid-ocean ridge basalts (MORB) [32], but is similar to CaO/Al₂O₃ found for typical medium-K basaltic andesites (CaO/Al₂O₃=0.46 for 648 samples; table 5.1 of [30]). If this reflects magmatic values, it suggests that a Ca-bearing, Al-free phase such as clinopyroxene controlled fractionation.

The samples are enriched in alkaline earth-incompatible elements Ba (365–800 ppm; mean=615 ppm) and Sr (700–1050 ppm; mean=871 ppm). The suite has a moderately low K/Rb (138–519; mean=377); much of this variability may reflect alteration. Compositional data for major elements, alkali metals, and alkaline earths suggest that the dykes behaved for the most part as closed systems during metamorphism. Because REE are considered to be less mobile than these elements in the metamorphic environment that these rocks experienced, REE patterns are unlikely to reflect important alteration effects. This is supported by the fact that there is no evidence for important hydrothermal circulation, which can redistribute REE [33,34]. The schistose dykes are all strongly enriched in the light rare earth elements (LREE), with up to 80× chondritic abundances of La. The suite is also depleted in heavy rare earth elements (HREE), with 3–7× chondritic abundances of Yb (Fig. 5). Chondrite-normalized La/Lu ((La/Lu)_n) range from 11 to 18, with a mean of 14. The REE patterns are characterized by minor or

no Eu anomalies. REE patterns indicate that a phase capable of fractionating LREE and HREE, such as garnet or amphibole, was important in magmatic evolution. This suggestion is supported by high Sr/Y (52–75; mean=66). In spite of this, (La/Lu)_n do not vary with Mg#, as would be expected from amphibole- or garnet-controlled fractionation (Fig. 5, inset) so it is unlikely that the samples are related simply by fractionation. The fact that Sr/Y (which is vulnerable to alteration) and (La/Lu)_n (which is not) are similarly high suggests that Sr/Y mostly manifests magmatic compositions and not alteration effects. The REE patterns and Sr/Y strongly indicate that these melts must have evolved in equilibrium with one or more mineral phases that fractionated HREE from LREE and that plagioclase was not important.

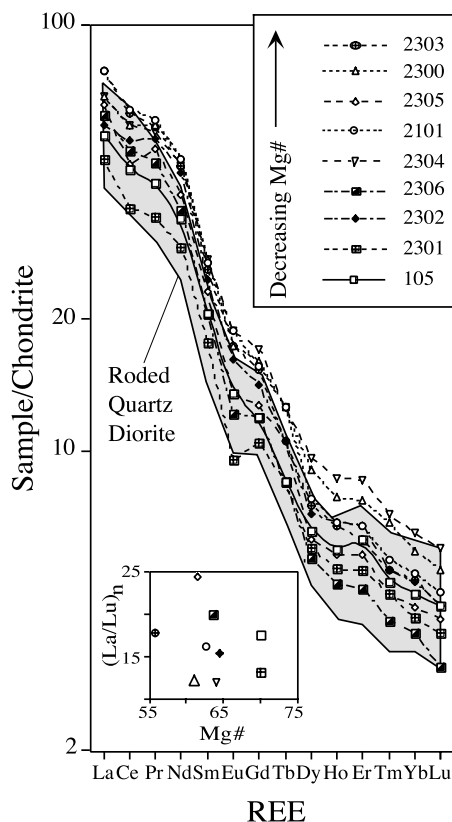


Fig. 5. Chondrite normalized REE patterns. Inset plots chondrite-normalized La/Lu ((La/Lu)_n) vs. Mg# for these samples. The gray field shows REE patterns of the Roded quartz diorite [44].

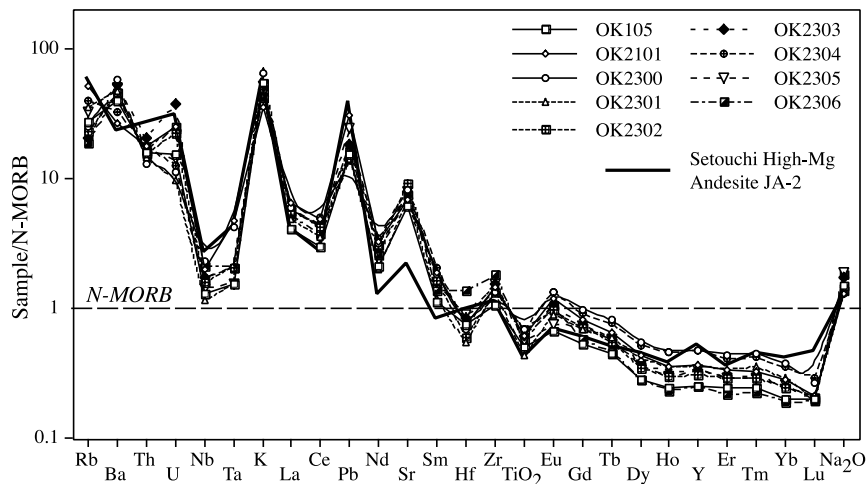


Fig. 6. Compatibility diagram of schistose dyke samples normalized to N-MORB [32]. Note strong enrichments in Rb, Ba, Th, U, K, Pb, and Sr and relative depletions in HFSE Nb, Ta, and Ti, typical of convergent margin magmas. This pattern is fundamentally indistinguishable from that of low-Ca boninite type 2 of [47], using the Geological Survey of Japan standard JA-2 (Miocene HMA from the Setouchi province of SW Japan).

The suite has low Nb/Zr (0.03–0.06; mean = 0.04), low Th/U (1.7–3.9; mean = 2.2), and high Ba/La (15–35; mean = 29) and Rb/Zr (0.13–0.44; mean = 0.27) typical of convergent margin magmatic suites. K/U varies significantly (4600–24,900) around a mean of 12,220. Although the mean value is remarkably like that for MORB (12,800 [35]), the scatter in K/U (and the fact that K/U varies with Th/U) suggests that alteration mobilized U.

The ‘spider diagram’ of element compatibility (Fig. 6) shows enrichments in Rb, Ba, Th, and U; a negative anomaly for Nb and Ta; positive anomalies for K, Pb, and Sr; and a modest negative anomaly in Ti. Alteration may be responsible for some of the variability seen in trace element contents, but on the whole, the consistency in patterns suggests that the magmatic signature is preserved. If we accept that the magmatic signature dominates over effects due to alteration, then the elemental patterns in Fig. 6 are best explained as characteristics of igneous rocks associated with active subduction zones [36]. These anomalies are caused by the addition of fluid-mobile elements (K, Rb, Ba, U, Sr, Pb) carried by fluids or melts released from the subducted slab and added to the mantle source of these melts. Depletions in high field strength (HSE) elements may be due to re-

sidual HSE-bearing phases or because the mantle source was already depleted [37]. These patterns are remarkably like those of the best-analyzed example of HMA as represented by a sample of Miocene Setouchi andesite (sanukite) from SW Japan (Geological Survey of Japan standard JA-2 <http://www.aist.go.jp/RIODB/geostand/igneous.html>).

Sr isotopic data are reported in Table 2. The samples have low $^{87}\text{Rb}/^{86}\text{Sr}$ (< 0.22), so corrections for 630 Ma of radiogenic growth are modest, allowing the calculation of meaningful initial $^{87}\text{Sr}/^{86}\text{Sr}$. These range from 0.70257 to 0.70347 (mean = 0.70305) and fall in the field previously defined for juvenile rocks of the ANS (Fig. 7). They are also indistinguishable from those of

Table 2
Sr isotopic data

Sample	$^{87}\text{Sr}/^{86}\text{Sr}$	$^{87}\text{Rb}/^{86}\text{Sr}$	Initial $^{87}\text{Sr}/^{86}\text{Sr}$
105	0.70467	0.145	0.70337
2101	0.70477	0.245	0.70257
2300	0.70379	0.100	0.70289
2301	0.70420	0.163	0.70274
2302	0.70405	0.080	0.70333
2303	0.70403	0.083	0.70329
2304	0.70413	0.156	0.70273
2305	0.70423	0.132	0.70304
2306	0.70420	0.081	0.70347

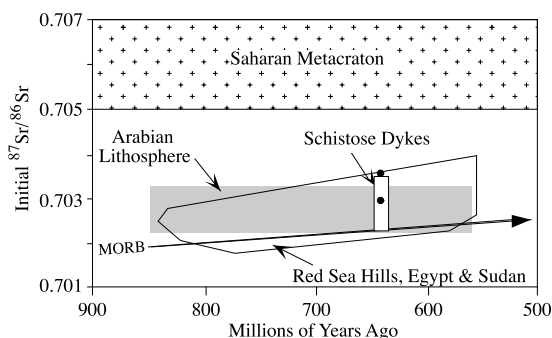


Fig. 7. Initial $^{87}\text{Sr}/^{86}\text{Sr}$ vs. age for the schistose dykes (the box encloses nine initial ratios from Table 2). Pre-Neoproterozoic crust of the Saharan Metacraton (west of the Nile) is shown as a radiogenic field (crosses). Lithospheric mantle beneath Arabia is shown in gray field. The solid line defines field for well-dated juvenile igneous rocks of Egypt and Sudan. The line with arrow approximates radiogenic growth of MORB-type asthenosphere; these fields are from [55]. Solid dots show initial $^{87}\text{Sr}/^{86}\text{Sr}$ for two samples of Roded quartz diorite [25].

the Roded quartz diorite (Fig. 7). There is no systematic variation of initial $^{87}\text{Sr}/^{86}\text{Sr}$ with Mg#. Some of this variability may reflect the effects of alteration, but because Nd and Hf isotopic compositions, which are less vulnerable to alteration, are also variable, we suspect that the variability in initial $^{87}\text{Sr}/^{86}\text{Sr}$ reflects that of the original igneous rocks.

Nd isotopic data are reported in Table 3. All samples had moderately positive initial ϵ_{Nd} , ranging from +2.7 to +4.9 (mean = +4.1). This indicates that the melts were derived from a source region that experienced long-term depletion in

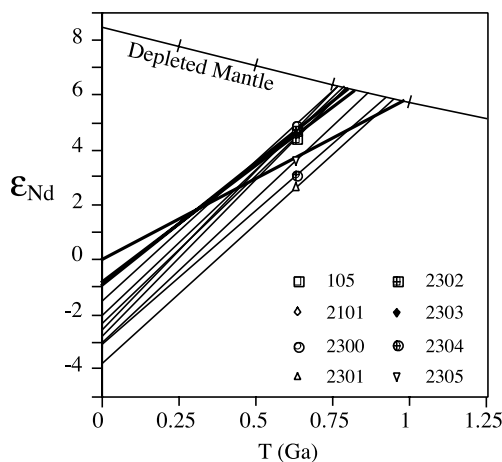


Fig. 8. Nd isotopic systematics for the schistose dykes. Depleted mantle model is from [39]. Thick solid lines (without symbols) represent trajectories for three samples of Roded quartz diorite analyzed in [25].

LREE, in spite of the fact that the samples are now strongly enriched in LREE. These values are indistinguishable from the initial ϵ_{Nd} of the Roded quartz diorite (range = +3.7 to +4.6; mean = +4.3) for three samples [25]. $^{147}\text{Sm}/^{144}\text{Nd}$ ranges from 0.095 to 0.12, well below the maximum value of 0.165 adopted for the calculation of meaningful Nd model ages [38]. Nd model ages calculated according to the depleted mantle model of Nelson and Depaolo [39] are in the range of 0.77–0.92 Ga (Fig. 8), similar to the mean model age of 0.80 ± 0.10 Ga for basement rocks of Sinai, Israel, and Jordan [38], and indistinguishable from Nd model ages for the Roded quartz diorite of 0.82–0.99 Ga. Given that these model ages are found for primitive as well as fractionated samples (including the quartz diorite), this must reflect the mantle, perhaps lithospheric, source and is not due to crustal contamination. Lu–Hf concentration and Hf isotopic data are reported in Table 4. Samples have $^{176}\text{Lu}/^{177}\text{Hf}$ that ranges from 0.061 to 0.112, significantly greater than the bulk earth value of 0.033 [40]. Samples have initial ϵ_{Hf} values which range from +6.8 to +8.8. These plot in the field for juvenile crust (Fig. 9), although at a significantly lower ϵ_{Hf} and ϵ_{Nd} part of the field than is occupied by other samples of the ANS.

Table 3
Whole rock Sm–Nd isotopic data

Sample	Sm	Nd	$^{147}\text{Sm}/^{144}\text{Nd}$	$^{143}\text{Nd}/^{144}\text{Nd}$	$\epsilon_{\text{Nd}}(630)$	T_{DM}
	(ppm)	(ppm)				(Ga)
105	4.20	23.76	0.1069	0.512516 ± 14	+4.7	0.77
2101	6.99	36.88	0.1146	0.512543 ± 10	+4.6	0.79
2300	6.83	35.00	0.1180	0.512573 ± 6	+4.9	0.77
2301	4.36	22.57	0.1168	0.512455 ± 12	+2.7	0.94
2302	6.17	34.65	0.1076	0.512503 ± 8	+4.4	0.80
2303	6.06	32.35	0.1132	0.512529 ± 10	+4.4	0.80
2304	7.70	38.72	0.1202	0.512491 ± 13	+3.1	0.92
2305	5.87	30.91	0.1148	0.512494 ± 9	+3.6	0.87
2306	5.15	28.70	0.1085	0.512500 ± 16	+4.3	0.81

Table 4
Whole rock Lu–Hf isotopic data

Sample	Lu (ppm)	Hf (ppm)	$^{176}\text{Lu}/^{177}\text{Hf}$	$^{176}\text{Hf}/^{177}\text{Hf}$	$(^{176}\text{Hf}/^{177}\text{Hf})_i$	$\epsilon_{\text{Hf}}(630)$
105	0.117	2.23	0.0074	0.282698 ± 8	0.282608	+8.6
2101	0.124	2.24	0.0078	0.282662 ± 11	0.282567	+7.1
2300	0.155	2.05	0.0106	0.282720 ± 23	0.282590	+7.9
2301	0.119	1.61	0.0104	0.282686 ± 25	0.282559	+6.8
2303	0.116	2.49	0.0065	0.282652 ± 29	0.282575	+7.3
2304	0.173	2.17	0.0112	0.282752 ± 16	0.282615	+8.8
2305	0.116	2.65	0.0061	0.282680 ± 11	0.282605	+8.5
2306	0.113	4.03	0.0039	0.282645 ± 25	0.282597	+8.2

5. Discussion

5.1. Fractionation of schistose dyke magmas

The schistose dykes are fractionated to varying extents, from negligible fractionation for those with Mg# and Cr and Ni contents that indicate equilibrium with mantle peridotite (e.g. OK105 and OK2301) to those which experienced significant fractionation (e.g. OK2303 and many analyzed by [23]). Fractionation did not occur simply, in a closed system, as demonstrated by the absence of simple relationships between Mg# and $(\text{La}/\text{Lu})_n$ (Fig. 5, inset). Fractionation may have been accompanied by assimilation of crust or sediments, although Sr, Nd, and Hf isotopic compositions do not vary systematically with Mg# and thus are difficult to relate simply to assimilation in the crust.

REE patterns and Sr/Y of the schistose dykes indicate that an important role in the evolution of these magmas was played by a phase capable of fractionating HREE and LREE. Two obvious candidates are amphibole and garnet [41,42]. A role for amphibole is indicated for the schistose dykes because of petrographic evidence that it was a liquidus phase, whereas garnet is not observed in thin sections. It is possible that garnet control was imposed upon melting (residual garnet). High Sr/Y and a lack of significant Eu anomalies suggests that plagioclase was not important in controlling fractionation of the suite. Mg# does not vary systematically with Sr/Y nor does Mg# vs. $(\text{La}/\text{Lu})_n$, further suggesting that shallow fractionation is not responsible for ele-

vated Sr/Y and $(\text{La}/\text{Lu})_n$. This suggests that these characteristics were largely established at the site of melt generation in the mantle.

An important clue to the fractionation history of schistose dyke magmas comes from the Roded quartz diorite (Fig. 1C). This pluton is intimately associated in space and time with the dykes and these share petrographic similarities. The quartz diorite is a greenish-gray, coarse-grained homogeneous rock, consisting of quartz (~10%), oligoclase ($\text{An}_{20}\text{--}\text{An}_{30}$; ~45%), biotite (~20%), hornblende (~20%), microcline (~5%) and sphene (~1%), with accessory apatite, zircon and epidote [43,44]. Quartz diorite mineralogy is similar to the modes and norms of the schistose dykes, although the former is more fractionated.

Dykes and pluton also show compositional affinities. The quartz diorite is generally more sili-

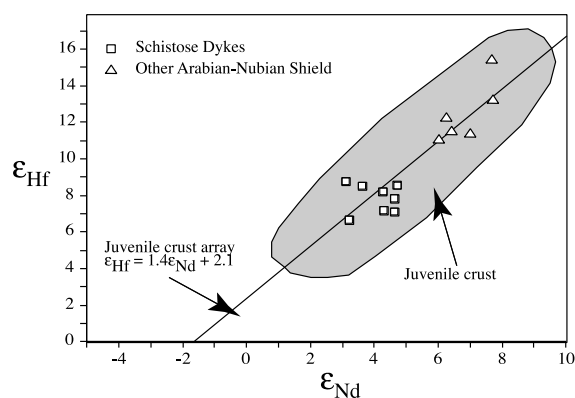


Fig. 9. Hf–Nd isotopic systematics. The field and regression line for juvenile crust after [56]. Data for other samples from the ANS from [56].

ceous than the schistose dykes, but still has relatively high Mg# (59), Ni (~ 100 ppm), and Cr (~ 90 ppm, Table 4). The ‘mean Roded quartz diorite’ in Table 5 falls along trends defined by the schistose dykes on plots of K vs. silica and FeO*/MgO vs. silica (Fig. 3), and for Mg# vs. Cr and Ni (Fig. 4). REE patterns are similar between quartz diorite and schistose dykes, and the quartz diorite, like the schistose dykes, shows little negative Eu anomaly (Fig. 5) [44]. Sr and Ba contents, Sr/Y and chondrite-normalized La/Yb ($(\text{La/Yb})_n$) are similarly high for quartz diorite

and schistose dykes (Table 5). Initial isotopic compositions of Sr and Nd are also similar (Figs. 7 and 8).

We conclude from the intimate association in space and time and compositional similarities that the schistose dykes and the Roded quartz diorite are different phases of the same igneous event, and so constitute important components of a system that we call the ‘Roded magmatic cell’. We further conclude that it is impossible to understand the fractionation of the pluton without understanding the dyke (and vice versa), in particular the role of garnet vs. amphibole in controlling fractionation. A critical aspect will be understanding the relationship between amphibolites in the region and the pluton. Some of these could be cumulates, for example those along the margins of the quartz diorite (Fig. 1C).

Another important issue is whether the dykes fed into the magmatic body now represented by the quartz diorite, or issued from it. Relationships between dykes and pluton in the field show comingling and other indications that these molten bodies were co-magmatic, but the details await resolution. The fact that the dykes are usually more primitive than the Roded quartz diorite suggests that the dykes fed into the evolving magmatic cell, but it is also possible that they emanated from it during an earlier stage in its evolution. The question of whether or not there are systematic compositional differences between concordant and discordant dykes needs to be answered.

The consanguineous relationship between the Roded quartz diorite and the schistose dykes illuminates the question of whether or not the former is an adakite. Adakites are dacitic rocks that are interpreted to form by melting of young and hot subducted oceanic crust [45]. The Roded quartz diorite is compositionally similar to the mean adakite of Martin [45], as shown in Table 5, including having high Sr/Y and $(\text{La/Yb})_n$ (Fig. 10). It has been interpreted as representing an adakite melt [44], but because it has a higher Mg# and Cr and Ni contents than typical adakites, these authors concluded that the adakite melt hybridized with mantle peridotite. The schistose dyke samples are andesitic and so cannot be adakites, but their ori-

Table 5

Compositional comparisons of schist dyke, Roded quartz diorite, HMA, and adakite

Element	HMA ^a	Primitive schist dyke OK105	Mean Roded schist dyke	Mean Roded quartz diorite ^b	Adakite ^c
SiO ₂	57.68	58.06	59.29	62.75	64.66
TiO ₂	0.67	0.81	0.98	0.79	0.51
Al ₂ O ₃	15.75	14.36	15.27	16.17	16.77
Fe ₂ O ₃	6.40	6.72	6.45	5.26	4.20
MnO	0.11	0.08	0.08	0.07	0.08
MgO	7.77	8.05	5.86	3.85	2.20
CaO	6.43	6.01	5.86	4.57	5.00
Na ₂ O	3.11	3.87	3.99	4.51	4.09
K ₂ O	1.81	1.73	1.64	1.86	1.72
P ₂ O ₅	0.15	0.31	0.57	0.16	0.17
Total	100	100	100	100	100
K ₂ O/Na ₂ O	0.58	0.45	0.41	0.41	0.42
Mg#	70.6	70	64.3	59.2	50.9
Ni (ppm)	130	250	143	104.8	24
Cr	436	450	264	93	36
Zr	116	110	149		
Nb	9.47	5	5.9	11.2	
Y	18.5	11	12	10	10
Sr	248	690	801	909	706
Rb	72.9	38	37.4	36.4	
Ba	321	565	671	690	
La	15.8	17	19.9	18.8	
Yb	1.62	0.97	1.02	0.93	0.93
Th	5.0	3.4	3.9	2.9	
Sr/Y	13.4	63	67	93	69
(La/Yb) _n	6.6	11.8	13.2	13.7	14.2

All values recalculated to 100% anhydrous.

^a Setouchi HMA Ja-2 <http://www.aist.go.jp/RIODB/geo-stand/semiment.html>.

^b Mean from [44], except for Cr [43].

^c Mean from [45].

gin may be closely related to that of adakites, as discussed below.

5.2. Petrogenesis of schistose dyke melts

The schistose dykes represent a magma type with the most primitive components of which were in equilibrium with mantle peridotite, in spite of having silica contents that correspond to basaltic andesite and andesite (Fig. 3, top panel). This is demonstrated by Mg# up to 70 or greater and concentrations of up to 250 ppm Ni and 450 ppm Cr in our samples. These can be classified as ‘high-mg andesites’ [46]. The schistose dyke suite is also remarkably similar in chemical composition to recent analytical data for suites identified as low-Ca type 2 boninite [47], as shown in Figs. 3, 4, and 6 and Table 5. Regardless of the name used to identify the schistose dyke magma type, the more primitive dykes clearly were primary melts in equilibrium with mantle peridotite.

There is a broad consensus that HMA and boninites only form in association with active subduction [46,48]. This is further supported by trace element patterns, which show the characteristic enrichments in fluid-mobile LIL elements and depletions in HFSE of subduction related igneous rocks (Fig. 6). Schistose dyke magmas clearly were generated by processes related to an active subduction zone about 630 Ma ago.

There is consensus about several important aspects of the petrogenesis of HMA magmas, which can be applied to understanding the generation of schistose dykes primary melts. The two occurrences of low-Ca type 2 boninites that Crawford et al. [47] used as examples are HMA of the Setouchi volcanic field, SW Japan and ‘Bajaaites’ from Baja California [49]. Both settings involved subduction of very young and hot oceanic lithosphere. Igneous activity of the Setouchi belt followed subduction of newly formed oceanic lithosphere of the Shikoku Basin and began about 17 Ma ago [50]. These erupted in the forearc region and are associated with younger adakites farther from the trench. The Bajaaites resulted from subduction of the Farallon–Pacific ridge off the coast of northern Baja California about 13 Ma [49].

The origin of the Setouchi HMAs has been

studied most closely, and this has similarities with the origin of adakitic melts. Adakites are thought to form by melting of young, hot subducted oceanic crust, in equilibrium with residual garnet [45]. Setouchi HMAs are thought to result from interaction of siliceous melts with mantle peridotite [46]. Shimoda et al. [51] suggest that melting of oceanic sediments produced the silicic melts which interacted with mantle peridotite to form the Setouchi source region. This melt rose into and interacted with overlying mantle peridotites. Experiments on hybridized mantle peridotite indicate that andesitic melts may be produced at relatively low temperatures [52] (1050–1100°C). It is noteworthy that the Setouchi HMA listed in Table 5 do not have high Sr/Y and $(La/Yb)_n$,

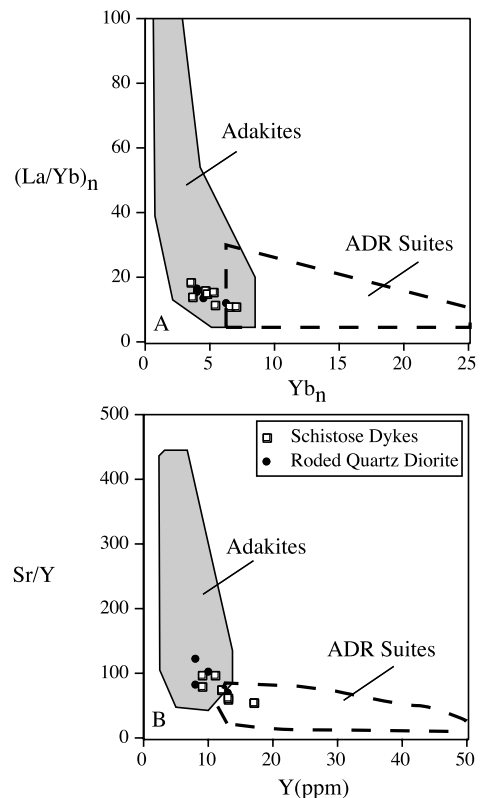


Fig. 10. Diagram showing differences between adakitic and andesite–dacite–rhyolite (ADR) suites that form by low-pressure fractionation of mafic melts. (A) Chondrite-normalized La/Yb $((La/Yb)_n)$ vs. chondrite-normalized Yb contents (Yb_n). (B) Sr/Y vs. Y (ppm). Both figures modified after [45]. Note that schistose dyke and Roded quartz diorite samples cluster in the field for adakites.

and may not have been in equilibrium with residual garnet. The petrogenetic model proposed for the Bajaites is very similar, with dacitic melts reacting with mantle peridotite to yield a hybridized melt source [49]. The principal difference between Bajaites and Setouchi HMA is that the subducted oceanic crust, not sediments, that melted to generate siliceous melts, and that melting occurs when the spreading ridge is subducted, terminating the subduction zone and allowing the mantle to isostatically rebound and decompress [49]. In addition, Bajaites have high Sr/Y and $(\text{La/Yb})_n$ indicating equilibrium with residual garnet. Generation of schistose dyke magmas is thought to be most similar to generation of the Bajaites.

5.3. Tectonic significance

The most important tectonic conclusion from this study is that HMA melts were generated about 632 Ma in the northernmost EAO, requiring a subduction zone existed beneath the northernmost EAO at least as late as ~ 632 Ma ago. This further requires that terminal collision between portions of East and West Gondwanaland to form the northernmost EAO occurred after this time, estimated from $^{40}\text{Ar}/^{39}\text{Ar}$ to have occurred in the northernmost ANS at 620 ± 10 Ma [12]. It is possible that terminal collision began earlier than this farther south in the EAO. Chemical characteristics of the schistose dyke HMAs are most consistent with subduction of very young crust, most likely associated with a spreading ridge of the Mozambique Ocean itself. Subduction of this ridge may have been the final event in closing the Mozambique Ocean, just before terminal collision between portions of East and West Gondwanaland began.

6. Conclusions

The schistose dykes of southern Israel are important representatives of subduction-related magmatism of ~ 632 Ma age in the northernmost part of the EAO. These magmas had silica contents corresponding to basaltic andesites and andesites but had Mg# as well as Ni and Cr con-

tents indicating equilibrium with mantle peridotite. They are a medium-K, calc-alkaline suite, strongly enriched in LREE and depleted in HREE. They are clearly HMAs and are very similar to low-Ca type 2 boninites and HMAs of the Setouchi volcanics of SW Japan. An intimate relationship with a nearby quartz diorite is indicated, although it is not clear whether the dykes represent magma that fed into a magma body now filled with the quartz diorite, or issued from it. Most likely these magmas reflect unusual processes of subduction zone melt generation resulting from subduction of a spreading ridge. The generation of boninitic magma at 630 Ma requires an active and probably quite juvenile subduction zone. This further indicates that collision between components E. and W. Gondwana to destroy the Mozambique Ocean and, ultimately, to create the end-Neoproterozoic supercontinent of Greater Gondwanaland or Pannotia must have occurred more recently than ~ 632 Ma.

Acknowledgements

This paper is dedicated to the memory of Yaacov Bendor, who pioneered the study of Precambrian basement of southern Israel, and who first studied the schistose dykes. L. Halicz (GSI) is thanked for the chemical analyses. This work was partly supported by GSI project 40082 and by the US–Israel BSF grant #2002337. Reviews by Joe Meert and Mark Reagan are gratefully acknowledged. **[Kf]**

References

- [1] R.J. Stern, Arc Assembly and Continental Collision in the Neoproterozoic East African Orogen Implications for the Consolidation of Gondwanaland, *Ann. Rev. Earth. Planet. Sci.* 22 (1994) 319–351.
- [2] S. Muhongo, A. Kröner, A.A. Nemchin, Single zircon evaporation and SHRIMP ages for granulite-facies rocks in the Mozambique Belt of Tanzania, *J. Geol.* 109 (2001) 171–189.
- [3] F.F. Bonavia, J. Chorowicz, Northward expulsion of the Pan-African of Northeast Africa guided by a reentrant zone of the Tanzania Craton, *Geology* 20 (1992) 1023–1026.

- [4] A. Segev, V. Goldshmidt, M. Rybakov, Late Precambrian–Cambrian tectonic setting of the crystalline basement in the northern Arabian–Nubian Shield as derived from gravity and magnetic data Basin-and-range characteristics, *Isr. J. Earth Sci.* 48 (1999) 159–178.
- [5] B. Blasband, S. White, P. Brooijmans, H. DeBoorder, W. Visser, Late Proterozoic extensional collapse in the Arabian–Nubian Shield, *J. Geol. Soc. Lond.* 157 (2000) 615–628.
- [6] A.S. Collins, T. Razakamanana, B.F. Windley, Neoproterozoic extensional detachment in central Madagascar; implications for the collapse of the East African Orogen, *Geol. Mag.* 137 (2000) 39–51.
- [7] M. Beyth, D. Avigad, H.-U. Wetzel, A. Matthews, S.M. Berhe, Crustal exhumation and indications for Snowball Earth in the East African Orogen north Ethiopia and east Eritrea, *Precambrian Res.* 123 (2003) 187–202.
- [8] M.I. Hussein, The Arabian Infracambrian extensional system, *Tectonophysics* 148 (1988) 93–103.
- [9] P. Hoffman, D. Schrag, The snowball Earth hypothesis Testing the limits of global change, *Terra Nova* 14 (2002) 129–155.
- [10] Z. Garfunkel, History and paleogeography during the Pan-African orogen to stable platform transition Reappraisal of the evidence from the Elat area and the Arabian–Nubian Shield, *Isr. J. Earth Sci.* 48 (1999) 135–157.
- [11] M. Beyth, R.J. Stern, R. Altherr, A. Kröner, The Late Precambrian Timna igneous complex. Southern Israel Evidence for comagmatic-type Sanukitoid monzodiorite and alkali granite magma, *Lithos* 31 (1994) 103–124.
- [12] M.A. Cosca, A. Shimron, R. Caby, Late Precambrian metamorphism and cooling in the Arabian–Nubian Shield: Petrology and $^{40}\text{Ar}/^{39}\text{Ar}$ geochronology of metamorphic rocks of the Elat area (southern Israel), *Precambrian Res.* 98 (1999) 107–127.
- [13] J.G. Meert, A synopsis of events related to the assembly of eastern Gondwana, *Tectonophysics* 362 (2003) 1–40.
- [14] N. Miller, M. Alene, R. Sacchi, R.J. Stern, A. Conti, A. Kröner, G. Zippi, Significance of the Tambien group (Tigray, N. Ethiopia) for Snowball Earth events in the Arabian–Nubian Shield, *Precambrian Res.* 121 (2003) 263–283.
- [15] A.F.M. Abdel-Rahman, Pan-African volcanism Petrology and geochemistry of the Dokhan Volcanic Suite in the northern Nubian Shield, *Geol. Mag.* 133 (1996) 17–31.
- [16] F.H. Mohamed, A.M. Moghazi, M.A. Hassanen, Geochemistry, petrogenesis and tectonic setting of late Neoproterozoic Dokhan-type volcanic rocks in the Fatira area, eastern Egypt, *Int. J. Earth Sci.* 88 (2000) 764–777.
- [17] A.M. Moghazi, Geochemistry and petrogenesis of a high-K calc-alkaline Dokhan Volcanic suite, South Safaga area, Egypt: the role of late Neoproterozoic crustal extension, *Precambrian Res.* 125 (2003) 161–178.
- [18] A. Fritz-Töpfer, Geochemical characterization of Pan-African dyke swarms in southern Sinai From continental margin to intraplate magmatism, *Precambrian Res.* 49 (1991) 281–300.
- [19] O. Katz, D. Avigad, A. Matthews, A. Heimann, Precambrian metamorphic evolution of the Arabian Nubian Shield in the Roded area, southern Israel, *Isr. J. Earth Sci.* 47 (1998) 93–110.
- [20] R.A. Bogoch, A. Gilat, D. Avigad, E. Zohar, M. Shiirav, L. Helicz, The Millstone gold anomaly, Roded prospect area: summary and evaluation, *Isr. Geol. Surv.*, 1990.
- [21] Y.K. Bendor, Petrographical outline of the Precambrian in Israel, *Bull. Res. Council Isr.* 10 (1961) 17–64.
- [22] A.E. Shimron, The Precambrian structural and metamorphic history of the Elat area, Ph.D. thesis, The Hebrew University of Jerusalem, 1972.
- [23] B. Cohen, A. Matthews, M. Bar-Matthews, A. Ayalon, Fluid-rock interaction in metamorphosed andesitic dikes, Elat metamorphic complex, Israel, *Isr. J. Earth Sci.* 49 (2000) 239–252.
- [24] A. Heiman, Y. Eyal, M. Eyal, K.A. Foland, Thermal events and low temperatures alteration in the Precambrian schistose dykes and their host rocks in the Elat area, southern Israel: $^{40}\text{Ar}/^{39}\text{Ar}$ geochronology, in: G. Bear, A. Heiman (Eds.), *Physics and Chemistry of Dykes*, A.A. Balkema, Rotterdam, 1995, pp. 281–292.
- [25] M. Stein, S. Goldstein, From plume head to continental lithosphere in the Arabian–Nubian Shield, *Nature* 382 (1996) 773–778.
- [26] M.J. LeBas, R.W. LeMaitre, A. Streckeisen, B.A. Zanettin, Chemical classification of volcanic rocks based on the total alkali–silica diagram, *J. Petrol.* 27 (1986) 745–750.
- [27] J.G. Pier, F.A. Podosek, J.F. Luhr, J.C. Brannon, J.J. Aranda-Gomez, Spinel-lherzolite-bearing Quaternary volcanic centers in San Luis Potosi, Mexico. 2. Sr and Nd isotopic systematics, *J. Geophys. Res.* B 94 (1989) 7941–7951.
- [28] J. Blichert-Toft, C. Chauvel, F. Albarede, Separation of Hf and Lu for high-precision isotope analysis of rock samples by magnetic sector-multiple collector ICP-MS, *Contrib. Mineral. Petrol.* 127 (1997) 248–260.
- [29] R.J. Arculus, Use and Abuse of the Terms Calcalkaline and Calcalkalic, *J. Petrol.* 44 (2003) 929–935.
- [30] J. Gill, *Orogenic Andesites and Plate Tectonics*, Springer, Berlin, 1981, 390 pp.
- [31] T. Plank, C.H. Langmuir, An evaluation of the global variations in the major element chemistry of arc basalts, *Earth Planet. Sci. Lett.* 90 (1988) 349–370.
- [32] A.W. Hofmann, Chemical differentiation of the Earth The relationship between mantle, continental crust, and oceanic crust, *Earth Planet. Sci. Lett.* 90 (1988) 297–314.
- [33] K.M. Gillis, J.N. Ludden, A.D. Smith, Mobilization of RE during crustal aging in the Troodos Ophiolite, Cyprus, *Chem. Geol.* 98 (1992) 71–86.
- [34] W. Bach, W. Irber, Rare earth element mobility in the oceanic lower sheeted dyke complex Evidence from geochemical data and leaching experiments, *Chem. Geol.* 151 (1998) 309–326.
- [35] K.P. Jochum, A.W. Hofmann, E. Ito, H.M. Seifert, W.M.

- White, K. U, and Th in mid-ocean ridge basalt glasses and heat production K/U and K/Rb in the mantle, *Nature* 306 (1983) 431–436.
- [36] R.J. Stern, Subduction zones, *Rev. Geophys.* 40 (2002) doi:10.1029/2001RG000108.
- [37] C.J. Hawkesworth, K. Gallagher, J.M. Hergt, F. McDermott, Mantle and Slab Contributions in Arc Magmas, *Ann. Rev. Earth. Planet. Sci.* 21 (1993) 175–204.
- [38] R.J. Stern, Crustal evolution in the East African Orogen a neodymium isotopic perspective, *J. Afr. Earth Sci.* 34 (2002) 109–117.
- [39] B.K. Nelson, D.J. DePaolo, Rapid production of continental crust 1.7 to 1.9 b.y. ago Nd isotopic evidence from the basement of the North American mid-continent, *Geol. Soc. Am. Bull.* 96 (1984) 746–754.
- [40] M. Bizarro, J.A. Baker, H. Haack, D. Ulfbeck, M. Rosing, Early History of Earth's crust-mantle system inferred from hafnium isotopes in chondrites, *Nature* 421 (2003) 931–933.
- [41] M. Klein, H.-G. Stosch, H.A. Seck, Partitioning of high field-strength and rare-earth elements between amphibole and quartz dioritic to tonalitic melts An experimental study, *Chem. Geol.* 138 (1997) 257–271.
- [42] M. Klein, H.-G. Stosch, H.A. Seck, N. Shimizu, Experimental partitioning of high field strength and rare earth elements between clinopyroxene and garnet in andesitic to tonalitic systems, *Geochim. Cosmochim. Acta* 64 (2000) 99–115.
- [43] V. Gutkin, Y. Eyal, Geology and evolution of Precambrian rocks, Mt. Shelomo, Mt. Elat area, *Isr. J. Earth Sci.* 47 (1998) 1–17.
- [44] R. Bogoch, D. Avigdad, T. Weissbrod, Geochemistry of the quartz diorite-granite association, Roded area, southern Israel, *J. Afr. Earth Sci.* 35 (2002) 51–60.
- [45] H. Martin, Adakitic magmas Modern analogues of Archean granitoids, *Lithos* 46 (1999) 411–429.
- [46] P.B. Kelemen, Genesis of high Mg# andesites and the continental crust, *Contrib. Mineral. Petrol.* 120 (1995) 1–19.
- [47] A.J. Crawford, T.J. Falloon, D.H. Green, Classification, petrogenesis and tectonic setting of boninites, in: A.J. Crawford (Ed.), *Boninites and Related Rocks*, Cambridge University Press, Cambridge, 1989, pp. 1–49.
- [48] N. Arndt, Komatiites, kimberlites, and boninites, *J. Geophys. Res.* 108 (2003) doi:10.1029/2002JB002157.
- [49] A.D. Saunders, G. Rogers, G.F. Marriner, D.J. Terrell, S.P. Verma, Geochemistry of Cenozoic Volcanic Rocks, Baja California, Mexico Implications for the Petrogenesis of Post-Subduction Magmas, *J. Volcanol. Geotherm. Res.* 32 (1987) 223–245.
- [50] J.I. Kimura, R.J. Stern, T. Yoshida, Re-initiation of subduction and magmatic responses in SW Japan during Neogene time, *J. Geodyn.*, submitted.
- [51] G. Shimoda, Y. Tatsumi, S. Nohda, K. Ishizuka, B.M. Jahn, Setouchi high-Mg andesites revisited geochemical evidence for melting of subducting sediments, *Earth Planet. Sci. Lett.* 160 (1998) 479–492.
- [52] K. Hirose, Melting experiments on lherzolite KLB-1 under hydrous conditions and generation of high-magnesian andesites, *Geology* 25 (1997) 42–44.
- [53] A. Peccerillo, S.R. Taylor, Geochemistry of Eocene calc-alkaline volcanic rocks from the Kastamonu area, northern Turkey, *Contrib. Mineral. Petrol.* 58 (1976) 63–81.
- [54] J.B. Miyashiro, Volcanic rock series in island arcs and active continental margins, *Am. J. Sci.* 274 (1974) 321–355.
- [55] R.J. Stern, A. Kroner, Late Precambrian crustal evolution in NE Sudan isotopic and geochronologic constraints, *J. Geol.* 101 (1993) 555–574.
- [56] J.D. Vervoort, J. Blichert-Toft, Evolution of the depleted mantle Hf isotope evidence from juvenile rocks through time, *Geochim. Cosmochim. Acta* 63 (1999) 533–556.